Resonant optical tunnel effect through dielectric structures of subwavelength cross sections

Christian Girard

CEMES, UPR CNRS 8011, 29 rue Jeanne Marvig, Boîte Postale 4347, F-31055 Toulouse Cedex 4, France

Alain Dereux

Laboratoire de Physique, Optique Submicronique, ESA 5027 CNRS, Université de Bourgogne, Boîte Postale 400, 21011 Dijon, France

Christian Joachim

CEMES, UPR CNRS 8011, 29 rue Jeanne Marvig, Boîte Postale 4347, F-31055 Toulouse Cedex 4, France

We show that *optical tunnel effects* through elongated structures of subwavelength cross sections can be enhanced by the appropriate structuration of the local dielectric function. Even under total internal reflection, transfer channels can be excited to perform spatially confined photonic transfer between transparent media linked by such subwavelength structures. The optical properties of such systems are analyzed using field susceptibilities, also known as electromagnetic Green's dyadics, which determine both the *local density of photon states* and the *optical transmittance* of the system. Green's dyadics obtained by solving numerically a set of dyadic Dyson equations are applied to study the optical properties of subwavelength structures connecting two semi-infinite materials. [S1063-651X(99)12005-1]

I. INTRODUCTION

In modern optical communication technologies, transferring optical energy from one dielectric medium to another is achieved by an optical waveguide connection. Such devices guide optical waves with low loss over very large distances. Most waveguides developed up to now have the following characteristics.

(i) Similar topology: a *core* is surrounded by one or several layers. The guiding properties mostly rely on the core. The surrounding layers ensure several functionalities from the optimization of the guiding properties to the mechanical and thermal protection of the device. The typical diameter of the core is of several micrometers. The smallest *core diameter* expected on the basis of the Rayleigh criterion [1] is of the *order of the incident wavelength* λ. For transverse sizes smaller than λ, the incoming electromagnetic wave decays exponentially inside the guide along the direction of propagation (longitudinal axis of the guide).

(ii) An efficient coupling of light into such an optical waveguide requires a perfect *alignment* of the wave vector of the incoming wave with the longitudinal axis of the guide.

(iii) *Homogeneity* of the index of refraction along the longitudinal direction. This homogeneity must be conserved over large distances to ensure an optimal guiding efficiency.

The present work explores new routes to break the fundamental limits (i) and (ii) of today's optical waveguides. Indeed, we propose solutions to scale down the core diameters to subwavelength sizes and to enable nonaligned incoming beams to couple to the guide. In our case, such nonaligned incoming waves are evanescent surface waves which correspond to waves incoming with an angle of incidence larger than the angle for total reflection. We will show that breaking the above-mentioned limits (i) and (ii) has some impact on the propagation length. However, the drawback is only apparent since it is compatible with the actual trends towards the miniaturization of optical devices. Moreover, we found that overcoming the limits (i) and (ii) with dielectric materials implies also breaking the homogeneity condition (iii). This point of view is in agreement with the observations reported by Joannopoulos [2]. These authors demonstrated that breaking the homogeneity condition (iii) brings new interesting properties to optical waveguides which still respect the conditions (i) and (ii).

When describing the propagation of light in ordered or partially ordered mesoscopic material structures [thus breaking the homogeneity condition (iii)], both the radiative and evanescent components of the electromagnetic field must be accounted for. For a given band of frequencies, the decay range of evanescent waves may be commensurate with the material structure or with parts of it. In this case, high values of the transmission coefficient of the electromagnetic energy can be expected. In other words, the overlap of evanescent components generated by two material structures or defects establishes the physical link that can open new optical channels. Impressive demonstrations of such collective proximity effects were extensively described in the recent literature dealing with photonic crystals [3–5]. This literature mostly presents a point of view similar to solid state physics where one focuses on the process of creating band *gaps* in a transparent reference medium rather than on the process of creating transmission bands in an opaque medium on which we focus in this paper.

As it may be intuitively understood, such periodic or pseudoperiodic materials modulate drastically the amount of transferred energy as a function of the incident frequency. For example, it was demonstrated both theoretically and experimentally that the introduction of well-calibrated microcavities inside a channel waveguide modulates the optical transmittance of an initially homogeneous waveguide [2]. The result of the modulation may be viewed as a photonic band structure in which some localized states can be created

by adding localized defects in the periodic structure. Under the normal illumination condition of a propagating light beam aligned along the longitudinal axis of the channel waveguide, the introduction of new localized states can be used to create narrow transmission bands inside the photonic gaps.

In a different context, the optical tunneling effect is used to control the optical energy transfer between two transparent media in photon scanning tunneling microscopes [PSTM, also called STOM (scanning tunneling optical microscope)] [6], and the variety of configurations of scanning near-field optical microscopes (SNOM) [7]. It has been clearly identified that the PSTM setup provides images which are unambiguously related to the distribution of the intensity of electromagnetic waves close to surfaces [8] while the interpretation of SNOM images has been, up to now, much less straightforward. In PSTM experiments which probe locally the intensity of the optical near field, the sample deposited on a glass prism is illuminated in total internal reflection. This particular illumination mode is characterized by a typical exponential decay of the detected intensity when the detector is moved away from the sample surface [9–16]. The reduction of the tip to sample spacing below the tunneling decay length makes the energy transfer possible. This decay can be strongly modified by introducing some localized photon state inside the tunnel gap. This principle is similar to the resonant tunnel effect of electrons [17–19].

This paper presents a theoretical analysis of the application of this principle to the enhancement of photonic transfer through *subwavelength optical waveguide* (SOW) excited by a polarized surface evanescent wave. We demonstrate that the periodic structuration of the SOW index of refraction along an appropriate direction stimulates the transfer efficiency even if the SOW diameter is scaled down to a fraction of the incident wavelength. In Sec. II, we show that beyond a critical modulation of the index of refraction, a periodic variation of the said index opens a photonic transmission band. Moreover, a significant transfer of energy is associated with this photonic transmission band. In Sec. III, we will study the transmittance of a SOW inserted between two planar semi-infinite transparent materials and illuminated in total internal reflection (TIR) [20,21]. The two usual polarization modes transverse electric (TE) and transverse magnetic (TM) will be investigated. From a numerical point of view, the study of such a complex optical system is rather challenging: computational difficulties are associated with the awkward geometry and with the important role played by the evanescent states. For example, the strong localization of evanescent waves around nanometer scale structures increases the computing time and downgrades the stability of methods based on an expansion in the reciprocal space (i.e, using Fourier transforms). The today well-established formalism of classical field susceptibilities is much more suitable to solve Maxwell equations for the typical parameters of near-field optics. It turns out that this framework provides a conceptually simple access to the different quantities of interest: near-field maps, local density of state, and optical transmittance [22–25]. Moreover, the field susceptibilities determining both the local density of photon states (LDOS) and the optical transmittance of the system are obtained by a
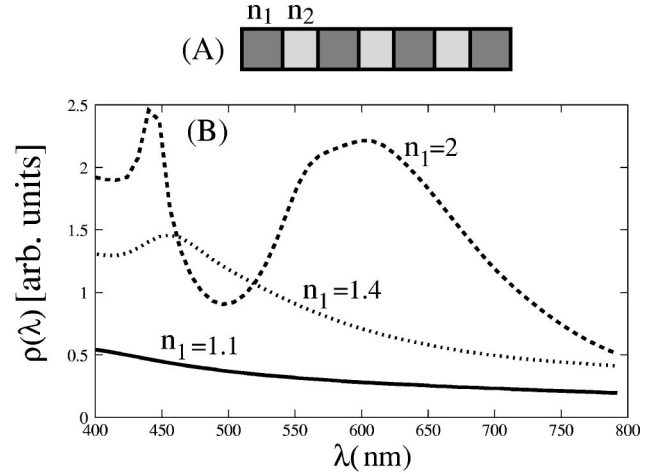
FIG. 1. (a) Heterowire geometry where $\sigma = 240$ nm, $N = 4$, $l_1 = 240$ nm, and $l_2 = 200$ nm resulting in a structure with a total length $L_0 = 1.560$ μm. (b) Variation of the integrated LDOS of different rod-shaped optical structures versus the excitation wavelength λ. The function $\rho(\lambda)$ is obtained by numerical integration of the photonic LDOS over the volume occupied by the rod described in (a). The three different curves have been obtained by increasing the modulation of the index of refraction $\Delta n = n_1 - n_2$. Solid curve, $\Delta n = 0$. Dotted curve, $\Delta n = 0.4$. Dashed curve, $\Delta n = 1$.

numerically stable solution of a set of dyadic Dyson equations.

II. SPECTRAL PROPERTIES OF OPTICAL HETEROWIRES

A. Optical heterowires

We define the heterowire geometry as a rod-shaped dielectric structure which displays a variation of the optical index of refraction along its longitudinal axis. Figure 1(a) shows an elementary heterowire made of only two materials setting up an alternating arrangement of N cells of optical index n_1 and and $N-1$ cells of optical index n_2. The respective lengths of the the cells along the longitudinal axis are l_1 and l_2. The cross section of the wire has a square shape of side σ. We will show later how this heterostructure can generate two photonic bands in the range of visible light.

Useful spectroscopic information can be extracted from the calculation of the LDOS $\eta(\mathbf{r}, \omega)$ of the wire. While it is well known in solid state physics [26], the use of the LDOS is not commonly spread in electrodynamics [27]. This scalar quantity is deduced from the electric field susceptibility (or Green's dyadic) $\mathbf{S}(\mathbf{r}, \mathbf{r}', \omega)$ of the heterowire

$$\eta(\mathbf{r}, \omega) = \frac{1}{\pi k_0^2} \text{Im Tr } \mathbf{S}(\mathbf{r}, \mathbf{r}, \omega) \tag{1}$$

where $k_0 = \omega/c$ is the wave vector modulus in vacuum and Im denotes the imaginary part. Solid state physics applies the concept of LDOS to nonrelativistic electrons so that the LDOS corresponds to the density of probability of finding an electron of energy $\hbar\omega$ at the point $\mathbf{r}$ of the solid. This function is directly related to the square moduli of all possible electronic wave functions associated with this energy. In the case of photons, different formulations of the LDOS can be

proposed depending on the reference field. The most widely used formulation relies on the calculation of the electric field susceptibility [Eq. (1)]. With this reference field, the LDOS is related to the square moduli of the electric field associated with all electromagnetic eigenmodes of frequency ω. When this quantity is defined on the basis of any kind of mixed field susceptibilities, such a straightforward relation to the electric field is not possible anymore. However, in any case, the LDOS is the only quantitative way to describe the continuous part of the spectrum of any system independently of the excitation mode. In the context of optics, this means that the LDOS provides spectroscopic information which is intrinsically independent of any particular illumination mode. As we will detail below, this independence allows us to separate unambiguously the optical properties of resonant optical structures and the side effects (such as interferences) generated by the incoming wave.

B. Field susceptibility of an optical heterowire

Within the framework of the linear response theory, the field susceptibilities provide the value of a field (electric or magnetic) at an observation point $\mathbf{r}$ and a pointlike source (dipolar or multipolar) located at $\mathbf{r}'$. Over the past 20 years, considerable works have been devoted to their theoretical analysis [28]. As indicated by Eq. (1), LDOS calculations require the knowledge of the electric field susceptibility of the system. This second rank tensor verifies the dyadic Dyson equation

$$\mathbf{S}(\mathbf{r},\mathbf{r}',\omega) = \mathbf{S_0}(\mathbf{r},\mathbf{r}',\omega)$$
$$+ \int_v \mathbf{S_0}(\mathbf{r},\mathbf{r}',\omega)\chi_{ow}(\mathbf{r}',\omega)\mathbf{S}(\mathbf{r},\mathbf{r}',\omega)d\mathbf{r}', \tag{2}$$

where $\mathbf{S_0}(\mathbf{r},\mathbf{r}',\omega)$ is the electric field susceptibility of the homogeneous medium surrounding the optical wire. This quantity has a simple analytical form

$$\mathbf{S_0}(\mathbf{r},\mathbf{r}',\omega) = \left(k_0^2 + \frac{1}{\epsilon_b(\omega)}\boldsymbol{\nabla}\boldsymbol{\nabla} \right)\mathcal{G}_0(\mathbf{r},\mathbf{r}',\omega), \tag{3}$$

where ϵ_b represents the optical dielectric constant of the surrounding medium and $\mathcal{G}_0$ is the scalar Green function of vacuum (see Ref. [27]). In Eq. (2), $\chi_{ow}(\mathbf{r}',\omega)$, the linear electric susceptibility of the optical heterowire is related to its optical index $n_{ow}(\mathbf{r})$ by the relation

$$\chi_{ow}(\mathbf{r}',\omega) = \frac{[n_{ow}(\mathbf{r}',\omega) - 1]}{4\pi}. \tag{4}$$

When dealing with complex optical systems such as those considered here, the precise resolution of Eq. (2) calls for particular attention. A recently developed numerical method solving the problem of electromagnetic scattering by nanoscopic structures [22,23] offers as a by-product a powerful tool for the calculation of the electromagnetic Green dyadic $\mathbf{S}$ of optical systems composed of several domains of arbitrary shape and optical indexes. In that framework, $\mathbf{S}$ is computed on the basis of the discretization of the Dyson equation (2):
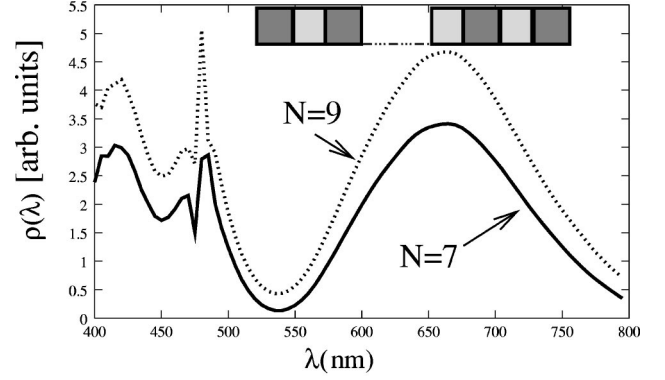
FIG. 2. For the same values of σ, l_1, and l_2 as in Fig. 1, variation of the integrated LDOS of two long rod-shaped optical structures versus λ for $N=7$ ($L_0 = 2.88\ \mu$m) and $N=9$ ($L_0 = 3.32\ \mu$m), respectively. The two curves have been computed for the same optical index contrast $\Delta n = 1.3$ resulting from the values $n_1 = 2.3$ and $n_2 = 1$.

$$\mathbf{S}(\mathbf{r}_i,\mathbf{r}_j,\omega) = \mathbf{S_0}(\mathbf{r}_i,\mathbf{r}_j,\omega)$$
$$+ \sum_{k=1}^{n} \chi_{k,ow}(\mathbf{r}_k,\omega)\mathbf{S_0}(\mathbf{r}_i,\mathbf{r}_k,\omega)\mathbf{S}(\mathbf{r}_k,\mathbf{r}_j,\omega), \tag{5}$$

where the volume of the optical heterowire has been divided into n meshes of volume V_k centered at $\mathbf{r}_k$, ($k=1,\ldots,n$), and

$$\chi_{k,ow}(\mathbf{r}_k,\omega) = [n_{ow}^2(\mathbf{r}_k,\omega) - 1]V_k/4\pi \tag{6}$$

is directly related to the value taken by the optical index at a given position $\mathbf{r}_k$ inside the optical heterowire. As an alternative to solving Eq. (5) with a standard linear algebra procedure, we apply the iterative procedure described in Ref. [22] which allows us to handle accurately very large discretized systems. Using Eq. (1), it is now possible to determine the density of electromagnetic eigenmodes by integrating the LDOS over the volume of the optical heterowire:

$$\rho(\omega) = \int_v \eta(\mathbf{r},\omega)d\mathbf{r}. \tag{7}$$

Due to the above-mentioned discretization, this last equation may be cast as

$$\rho(\omega) = \frac{1}{\pi k_0^2} \sum_{k=1}^{n} V_k \operatorname{Im} \operatorname{Tr} \mathbf{S}(\mathbf{r}_k,\mathbf{r}_k,\omega). \tag{8}$$

For a given system, a preliminary analysis of this function allows the photonic bands to be identified (see Figs. 1 and 2). Figure 1(b) provides a first numerical example of the evolution of the density of states of an optical heterowire versus its index modulation $\Delta n = n_1 - n_2$. The background index of refraction $n_b = \sqrt{\epsilon_b} = 1$. In this example, the second optical index n_2 is maintained constant with the same value as the background ($n_2 = 1$). Beyond a critical value of Δn, we observe the gradual formation of two photonic bands of eigenmodes centered on $\lambda = 450$ nm and $\lambda = 600$ nm. Note that, in the context of this paper, we define a photonic band as a
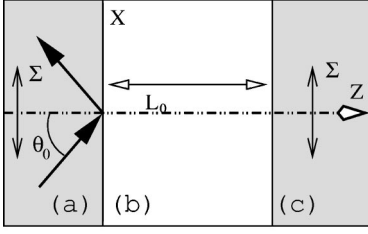
FIG. 3. Three dielectric media (indexes of refraction n_a, n_b, and n_c) arranged as a planar optical junction. L_0 is the thickness of the gap material (b). θ_0 defines the angle of incidence of the incoming wave in the *input* medium (a). Σ is the collecting area used for the integration of the Poynting vector in the *output* medium (c).

local increase of the DOS due to the coupling between localized photon states. Indeed, the two photonic bands of eigenmodes which show up for ($n_1 = 2$) in Fig. 1(b) are not separated by a true gap which would be characterized by a vanishing LDOS. Furthermore, since we are working with structures of finite dimensions, the heterowire cannot generate an *absolute* photonic band gap independent of the incident wave vector. Nevertheless, the LDOS describes quantitatively the continuous optical spectrum of the structure. The description is not entangled in the features of any particular illumination mode. Independently of the incoming wave, the LDOS can be used for operation research purposes when optimizing the geometrical parameters l_1 and l_2 as well as the optical index modulation of a structure.

In Fig. 2, we report similar calculations performed for two more elongated wires ($N = 7$ and 9). They will be the basis of the interpretation of the data of the next section. We can see that increasing the number of cells first broadens the photonic band centered on red wavelengths while shifting its maximum to 660 nm and, second, deepens the gap between 500 and 550 nm. This effect results from the coupling between the lower frequency eigenmodes supported by each dielectric cell. This can be checked by the comparison of the average effective wavelength inside the structure with the average wavelength of the band. This important point will be confirmed by the value of the optical transmittance.

III. SUBWAVELENGTH OPTICAL WAVEGUIDES

In this section, we introduce the concept of a *subwavelength optical waveguide* (SOW). A SOW is obtained by inserting an optical heterowire inside a reference system. This reference system is characterized by a photonic band gap where the optical transmittance vanishes. The insertion of the heterowire results in a SOW if it opens a transmission band in the photonic gap of the reference system.

A. An operational photonic band gap

The simplest reference system providing an operational, albeit incomplete, photonic gap is defined by the optical junction of Fig. 3 where three dielectric media (a), (b), and (c) are arranged in a planar geometry. Throughout the paper, this geometry will be considered as the reference system which defines not only the incident electromagnetic fields $\{\mathbf{E_0}(\mathbf{r}, \omega)$ and $\mathbf{B_0}(\mathbf{r}, \omega)\}$ but also to the initial field susceptibilities $\mathbf{S_0}$ and $\mathbf{Q_0}$. The indexes of refraction are such that

$n_c = n_a$ and $n_a > n_b$. When the angle of incidence θ_0 of the incoming wave is larger than the critical angle for total reflection θ_c, the reference system is in the so-called tunnel configuration because the transmittance T [defined by the normalized energy flux transmitted in the medium (c)] displays a quasiexponential decay with respect to L_0 [1] which can be approximated by

$$T(L_0) = A \exp[-\Gamma(\theta_0, k_0)L_0]. \quad (9)$$

The decay factor $\Gamma = 2[n_a^2 \sin(\theta_0)^2 - n_b^2]k_0$ depends on the angle of incidence θ_0. The factor A is determined by the polarization mode (s or p) illuminating the system. According to this simple relation, if L_0 grows beyond a few incident wavelengths, the amount of energy reaching the third medium (c) is not significant anymore. As stated above, the photonic band gap is incomplete because angles of incidence smaller than θ_c do not lead to the total internal reflection which is associated with optical tunneling. This tunneling phenomenon is exploited in the photon scanning tunneling microscope (PSTM) [6] which was inspired by the electron scanning tunneling microscope (STM) [29]. In the context of electron physics, structuring the barrier of potential either with an atomic [30], or a molecular wire [31], made it possible to control the mechanisms governing this exponential decay of the tunneling regime [32].

B. Transmittance of a heterowire

What happens when a heterowire connects the input (a) and output (c) media of the above described reference system? The incoming evanescent electric and magnetic fields $\mathbf{E}_0(\mathbf{r}, \omega)$ and $\mathbf{B}_0(\mathbf{r}, \omega)$ are scattered by the heterowire structure. As demonstrated in Refs. [25,23], the resulting electromagnetic fields $\{\mathcal{E}(\mathbf{r}, \omega), \mathcal{B}(\mathbf{r}, \omega)\}$ can be computed anywhere by introducing two generalized propagators labeled $\mathcal{K}(\mathbf{r}, \mathbf{r}', \omega)$ and $\mathcal{L}(\mathbf{r}, \mathbf{r}', \omega)$, respectively. Since throughout all the paper the heterowire is assumed to respond linearly to excitations, the resulting electric and magnetic fields are described by the following linear relations:

$$\mathcal{E}(\mathbf{r}, \omega) = \int_v \mathcal{K}(\mathbf{r}, \mathbf{r}', \omega)\mathbf{E}_0(\mathbf{r}', \omega)d\mathbf{r}' \quad (10)$$

and

$$\mathcal{B}(\mathbf{r}, \omega) = \int_v \mathcal{L}(\mathbf{r}, \mathbf{r}', \omega)\mathbf{E}_0(\mathbf{r}', \omega)d\mathbf{r}' \quad (11)$$

with

$$\mathcal{L}(\mathbf{r}, \mathbf{r}', \omega) = \frac{\delta(\mathbf{r} - \mathbf{r}')}{ik_0}\Lambda'_{\mathbf{r}}$$
$$+ \int_v \mathbf{Q}_{\text{junc}}(\mathbf{r}, \mathbf{r}', \omega)\chi_{ow}(\mathbf{r}'', \omega)\mathcal{K}(\mathbf{r}'', \mathbf{r}', \omega)d\mathbf{r}'',$$
$$(12)$$

where $\Lambda'_{\mathbf{r}}$ labels the matrix form of the curl operator. The dyadic $\mathbf{Q}_{\text{junc}}(\mathbf{r}, \mathbf{r}', \omega)$ represents the mixed *electric-magnetic propagator* (EMP) of the reference junction. The integrals run over the volume v of the heterowire. As detailed in Ref.

[22], the generalized electric field propagator $\mathcal{K}(\mathbf{r},\mathbf{r}',\omega)$ can be formulated using the electric Green dyadic $\mathcal{S}(\mathbf{r},\mathbf{r}',\omega)$ associated with the complete geometry (heterowire added to the reference system):

$$\mathcal{K}(\mathbf{r},\mathbf{r}',\omega)=\delta(\mathbf{r}-\mathbf{r}')+\mathcal{S}(\mathbf{r},\mathbf{r}',\omega)\chi_{ow}(\mathbf{r}',\omega). \quad (13)$$

The dyadic $\mathcal{S}(\mathbf{r},\mathbf{r}',\omega)$ is obtained numerically through the same Dyson equation (5) (the one used to compute the LDOS of the isolated wire) where we replace the reference dyadic $\mathbf{S}_0$ by

$$\mathbf{S}_{junc}(\mathbf{r},\mathbf{r}',\omega)=\mathbf{S}_0(\mathbf{r},\mathbf{r}',\omega)+\mathbf{S}_{a,c}(\mathbf{r},\mathbf{r}',\omega), \quad (14)$$

where the dyadic $\mathbf{S}_{a,c}$ added to $\mathbf{S}_0$ accounts for the presence of both input and output media. The analytical formulation of the contribution $\mathbf{S}_{a,c}$ can be deduced from a pioneering paper by Agarwal (Ref. [27]). A variety of numerical techniques available in the literature allow us to evaluate such a response function.

The values of the electric $\mathcal{E}(\mathbf{r},\omega)$ and magnetic $\mathcal{B}(\mathbf{r},\omega)$ fields transmitted in the output medium (c) yield the time-average Poynting vector field

$$\mathcal{P}(\mathbf{r})=\frac{1}{2}\text{Re}\{\mathcal{E}(\mathbf{r},\omega)\wedge\mathcal{B}^*(\mathbf{r},\omega)\}. \quad (15)$$

The power crossing the surface Σ located inside the input medium and centered around the SOW (Fig. 3) is given by the flux of the Poynting vector through Σ. The normalization of this power by the incident power p_{inc} crossing the same surface Σ defines the transmission coefficient of the heterowire

$$T(L_0,\theta_0,\lambda)=\frac{\int_{\Sigma}\mathcal{P}(\mathbf{l},L_0+Z_{\Sigma})\mathbf{u_z}d\mathbf{l}}{p_{inc}}. \quad (16)$$

In this last equation, Z_{Σ} is the position of the surface Σ along the z axis in the *output* medium, $\mathbf{l}=(x,y)$, and $\mathbf{u_z}$ is a unit vector directed along the z axis. In the following, we apply this method in order to determine which kind of heterowire will result in a SOW. A good convergence of the numerical works was achieved by cubic cells having a side equal to 30 nm.

C. Homogeneous wire

For this application, the indexes of refraction of the two semi-infinite dielectric media n_a and n_c the function $n_{ow}(\mathbf{r})$ are kept at the constant value 1.5. For a typical length of the wire $L_0=2.88$ μm, the two curves in Fig. 4 clearly evidence the dramatic decay of the transmission coefficient versus the incident wavelength when $\sigma<\lambda$. As expected intuitively for σ in the subwavelength range, the absence of optically active modes in the waveguide prevents any significant energy transfer between the incident and the exit media. For example, around a typical wavelength of 640 nm and with σ reduced to 240 nm (solid curve), the coefficient $T(L_0,\theta_0,\lambda)$ falls down to 10^{-3}.
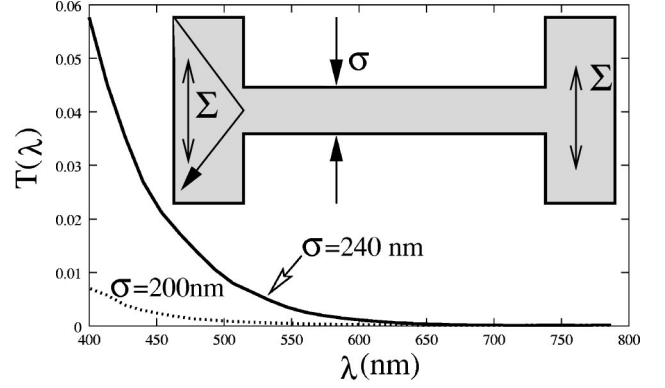
FIG. 4. Variation of the transmittance of a subwavelength homogeneous wire (see inset) as a function of the incident wavelength λ. The indexes of refraction $n_a=n_c=n_{ow}(\mathbf{r})=1.5$ and $L_0=2.88$ μm. The calculation has been made for the p-polarized mode of illumination with $\theta_0=46°$.

D. Periodic heterowire

An advantage of the formalism presented above lies in the fact that it handles complex heterogeneous systems formed by N distinct subdomains. In our second application, we use this opportunity to analyze the optical coupling of the two semi-infinite dielectric media n_a and n_c by the heterowires studied in Sec. II (see Fig. 2). These structures display an alternation of two different materials of optical indexes $n_{ow}^{(1)}$ and $n_{ow}^{(2)}$ (see inset of Fig. 5). As in Sec. II, the numerical
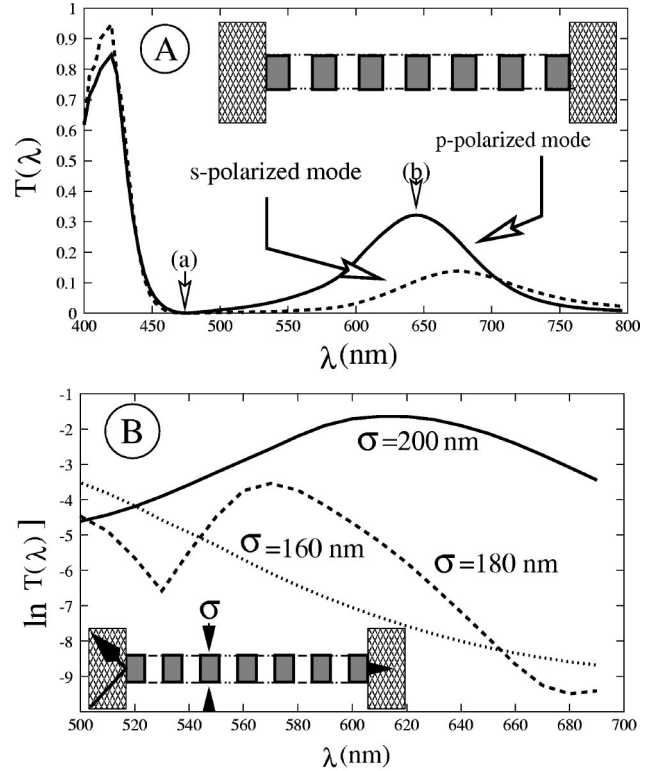
FIG. 5. (a) A periodic heterowire $\sigma=240$ nm ($l_1=240$ nm, $l_2=200$, $n_{ow}^{(1)}=1.0$, $n_{ow}^{(2)}=2.3$) replaces the homogeneous wire of Fig. 4. In the p-polarized mode, two bands of respectively weak (a) and strong (b) optical transparences show up in the transmission spectrum. (b) The dependence of the tunnel photonic band (b) on the transverse size σ. $\Sigma=0.25$ μm^2.
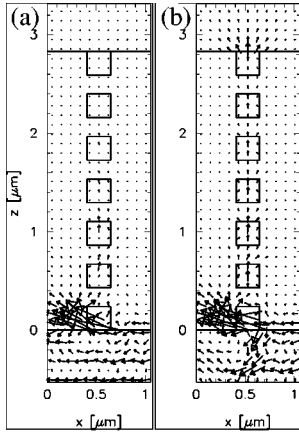
FIG. 6. Planar projection of the time-averaged Poynting $\mathcal{P}(x,y=cst,z)$ vector in a x-z plane cutting the center of the SOW defined in Fig. 5(a). The wavelengths are chosen by inspection of Fig. 5(a) so that $\lambda = 475$ nm (a) lies in the gap and and $\lambda = 640$ nm (b) lies in the transmission band.

applications are performed with $l_1 = 240$ nm, $l_2 = 200$ nm, and the indexes of refraction $n_{ow}^{(1)} = 1.0$ (air), $n_{ow}^{(2)} = 2.3$ (dielectric). Unlike the decay of the transmission coefficient observed at the exit of homogeneous wire (Fig. 4), the curves of Fig. 5(a) ($\sigma = 240$ nm) indicate a dramatic modification of the transmission spectrum. Although an exponential envelope still controls the transmission coefficient for visible wavelengths, two photonic transmission bands show up, enhancing the photonic transfer efficiency, respectively, around $\lambda_a = 425$ nm and $\lambda_b = 640$ nm. These two bands, where the optical tunnel effect occurs, agree with the LDOS of the isolated heterowire calculated previously in Sec. II. Since the insertion of the heterowire opens a transmission band in the operational photonic gap of the reference system, we conclude that this particular heterowire yields a SOW.

When we compare this spectrum to the LDOS of Fig. 2 (solid curve), we remark that a reduced set of eigenmodes is excited by the TIR illumination. In both s and p polarization modes, this selective effect, related to the particular illumination mode, tends to enlarge the apparent gap between the two photonic bands (a) and (b).

To complete this information, Fig. 6 displays a map of the energy flowing through the device for two typical wavelengths. For a wavelength chosen in the gap, no significant energy transfer occurs. The efficiency increases drastically if the wavelength corresponds to the center of the photonic band (b) of Fig. 5(a). This increasing energy flow is accompanied by an intriguing change of direction of the incident wave vector when the optical wire is excited near the resonance.

For visible wavelengths, the photonic bands considerably enhance the transfer process even for SOW with smaller transverse sizes. With $\sigma = 200$ nm, the enhancement around the second band (b) is about three orders of magnitude when passing from a homogeneous wire (dashed curve of Fig. 4) to the periodic heterowire [solid line in Fig. 5(b)]. We note that for the contrast of the index of refraction considered in this application ($\Delta n = n_{ow}^{(2)} - n_{ow}^{(1)} = 1.3$), the extinction of the transmission peak related to the band (b) occurs for SOW diameters smaller that 160 nm, i.e., when $\sigma < \lambda/4$.

At first sight, the SOW phenomenon could belong to a recently identified series of photonic crystal effects where light propagation is supported by bended lines of defects [4]. However, we can bring to the fore fundamental differences between SOW and photonic crystal effects.

(a) The SOW effect is created by simple modification of the vacuum LDOS produced by adding some localized photonic states. In photonic crystals, the role of defects must be understood relatively to the LDOS of an infinite periodic system. The calculation of the LDOS of photonic crystals is much more cumbersome than the simple LDOS of vacuum.

(b) In order to prevent the excitation of the delocalized vacuum states, a SOW is excited by an evanescent surface mode. This is fundamentally different from a photonic crystal which requires it to be excited by a radiative wave.

(c) The reduction of the SOW cross section to subwavelength scales still allows a transmission process. Up to now, photonic crystal effects have not offered this characteristic.

E. Light localization and resonant tunneling

The resonant electronic tunnel effect observed in various contexts of solid state physics (superlattices, quantum wells, localized defects in metal oxide metal junctions, . . .) is always accompanied by a localization of the electronic wave function in the tunnel barrier [17]. In photonics, a similar localization phenomenon may be expected. However, in the configuration analyzed in this paper, the radiative losses, induced by scattering along the wire, limit significantly the amplitude of this a phenomenon. To close our numerical analysis, we present in Figs. 7(a) and 7(b), both electric and magnetic field intensity maps $|\mathcal{E}(x,0,z)|^2$ and $|\mathcal{B}(x,0,z)|^2$ when the junction is excited by a light of incident wavelength $\lambda = 640$ nm, i.e., corresponding to the peak of the photonic band (b) in Fig. 5(a).

Near the resonance, the light field can display strong enhancement at the junction between the input medium (1) and the optical wire. In order to represent the field variations over all the device, a logarithmic scale has been chosen. These two maps, calculated in the p-polarized mode, reveal the perfect commensurability existing between the variations of field intensity along the longitudinal axis of the SOW and the modulation of the index of refraction. In particular, the seven magnetic field intensity maxima are precisely localized at the center of each cell of higher index of refraction. The electric field pattern displays more complex features, with peaks along the lateral faces of the cells of higher index of refraction. In both maps, complex fringe patterns show up. They are generated by interference between the incident surface evanescent wave and the wave scattered by the SOW. Finally, both maps reproduce the above-mentioned drastic change of direction of the energy flow.

IV. CONCLUSION AND PERSPECTIVE

The above theoretical framework, supported by numerical simulations, indicates that optical tunneling effects through subwavelength optical waveguides can be enhanced by an appropriate structuration of the index of refraction. Furthermore, even under total internal reflection, transmission channels could be excited to produce an efficient energy transfer. This effect can thus be exploited to perform otherwise for-
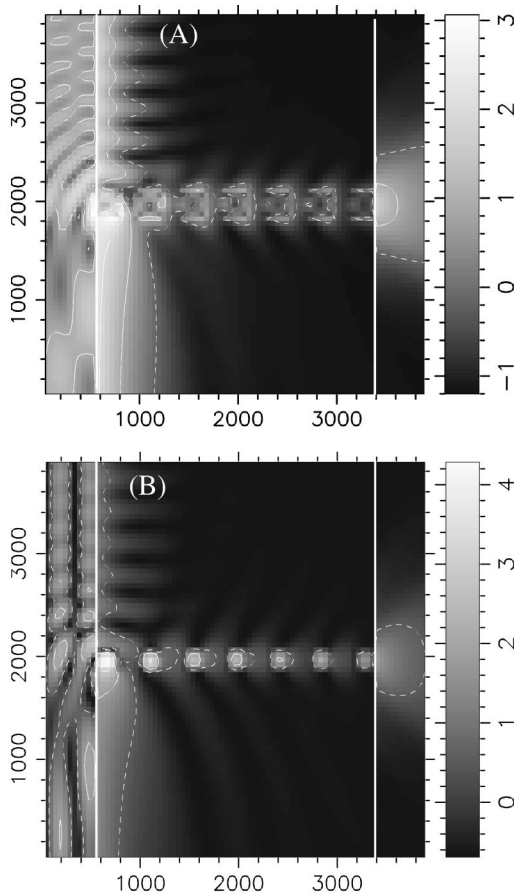
FIG. 7. Localization of light associated with the resonant optical tunneling effect (size: 4 μm$\times$4 μm). The calculation has been made for the incident wavelength $\lambda = 640$ nm. The computation window is in a plane x-z cutting the center of the SOW. (a) Map of the electric field intensity $I_{\mathcal{E}}(x,z) = \ln[\eta + |\mathcal{E}|^2(x,y=0,z)]$; (b) map of the magnetic field intensity $I_{\mathcal{B}}(x,z) = \ln[\eta + |\mathcal{B}|^2(x,y=0,z)]$. A logarithmic scale and the arbitrary parameter η, here fixed respectively to 0.3 and 0.5, are used to improve the visualization of the phenomena.

bidden photonic transfer between two arbitrary transparent media linked by a SOW. The optimization of this concept could lead to the realization of subwavelength optical devices that could be integrated in planar geometry. An attractive application of the concept lies in the possibility of ad-

dressing optically a region at the surface of a dielectric material with a large number of SOW which could be packed with a high density related to the subwavelength cross sections.

For each proposal, the development to a practical device requires the following.

(i) The identification of dielectric materials (indexes of refraction) which are pertinent to realizing the device.

(ii) The definition of the appropriate illumination mode leading to an excitation by an evanescent wave.

(iii) The optimization of geometrical parameters to open photonic transmission bands in the desired range of wavelengths (visible, near infrared, infrared). This optimization relying on numerical simulations will also be precious to define the characteristic operational wavelengths of the device.

Although a vertical growth process could be used to fabricate the SOW connecting transparent semi-infinite media discussed previously, the most reliable way *to check* the effects described above consists in the integration of the SOW in planar geometry. This option must be developed by incorporating the illumination medium on the same substrate. The numerical simulations of Figs. 1 and 2 indicate that the expected effects should occur beyond a certain index modulation. Consequently, if the SOW is composed alternately of air and dielectric cells, the optical index of the dielectric cells n_1 should range approximately between 2 and 3. Such contrasts are available by using the optical properties of the TiO$_2$, III-V semiconductor at wavelengths close to the absorption threshold and some based on silicon compounds. For example, both SiO$_x$ and SiN$_y$ are good candidates to fabricate nanostructures of high optical indexes on dielectric or silicon wafers [33].

[1] M. Born and E. Wolf, *Principles of Optics* (Pergamon, Oxford, 1975).

[2] J. D. Joannopoulos, P. R. Villeneuve, and S. Fan, Nature (London) **386**, 143 (1997).

[3] E. Yablonovitch, J. Mod. Opt. **41**, 173 (1994).

[4] J. D. Joannopoulos, R. Meade, and J. Winn, *Photonic Crystals* (Princeton Press, Princeton, NJ, 1995).

[5] P. R. Villeneuve, S. Fan, J. D. Joannopoulos, K. Lim, J. C. Chen, G. S. Petrich, L. A. Kolodziejski, and R. Reif, in *Photonic Band Gap Materials*, Vol. 315 of *NATO Advanced Study Institute, Series E: Applied Sciences*, edited by C.M. Soukoulis (Kluwer, Dordrecht, 1996), pp. 411–426.

[6] R. C. Reddick, R. J. Warmack, and T. L. Ferrell, Phys. Rev. B **39**, 767 (1989).

[7] D. Courjon and C. Bainier, Rep. Prog. Phys. **57**, 989 (1994).

[8] J. C. Weeber, E. Bourillot, A. Dereux, J. P. Goudonnet, Y. Chen, and Ch. Girard, Phys. Rev. Lett. **77**, 5332 (1996).

[9] J. M. Vigoureux, Ch. Girard, and D. Courjon, Opt. Lett. **14**, 1039 (1989).

[10] R. C. Reddick, R. J. Warmack, D. W. Chilcott, S. L. Sharp, and T. L. Ferrell, Rev. Sci. Instrum. **61**, 3669 (1990).

[11] T. L. Ferrell, S. L. Sharp, and R. J. Warmack, Ultramicroscopy **42-44**, 408 (1992).

[12] D. Courjon, C. Bainier, and M. Spajer, J. Vac. Sci. Technol. B **10**, 2436 (1992).

[13] F. de Fornel, L. Salomon, P. Adam, E. Bourillot, J. P. Goudonnet, and M. Nevière, Ultramicroscopy **42-44**, 422 (1992).

[14] N. F. van Hulst, F. B. Segerink, F. Achten, and B. B. Bölger, Ultramicroscopy **42-44**, 416 (1992).

[15] N. F. van Hulst, M. H. Moers, and B. Bölger, J. Microsc. **171**, 95 (1993).

[16] L. Salomon, F. de Fornel, and J. P. Goudonnet, J. Opt. Soc. Am. A **8**, 2009 (1991).

[17] S. Luryi, Appl. Phys. Lett. **47**, 490 (1985).

[18] F. W. Sheard and G. A. Toombs, Appl. Phys. Lett. **52**, 1228 (1988).

[19] M. Rahman and J. H. Davies, Semicond. Sci. Technol. **5**, 168 (1990).

[20] D. Courjon, C. Bainier, C. Girard, and J. M. Vigoureux, Ann. Phys. (Leipzig) **2**, 149 (1993).

[21] Ch. Girard, Phys. Rev. B **58**, 12 551 (1998).

[22] O. J. F. Martin, C. Girard, and A. Dereux, Phys. Rev. Lett. **74**, 526 (1995).

[23] Ch. Girard, J. C. Weeber, A. Dereux, O. J. F. Martin, and J. P. Goudonnet, Phys. Rev. B **55**, 16 487 (1997).

[24] Ch. Girard, O. J. F. Martin, and A. Dereux, Phys. Rev. Lett. **75**, 3098 (1995).

[25] Ch. Girard and A. Dereux, Rep. Prog. Phys. **59**, 657 (1996).

[26] E. Economou, *Green's Functions in Quantum Physics*, Springer Series in Solid State Science, 2nd ed. Vol. 7 (Springer, Berlin, 1983).

[27] G. S. Agarwal, Phys. Rev. A **11**, 230 (1975).

[28] H. Metiu, Prog. Surf. Sci. **17**, 153 (1982), and references therein.

[29] G. Binnig and H. Rohrer, Helv. Phys. Acta **55**, 726 (1982).

[30] A. Yazdani, D. M. Eigler, and N. D. Lang, Science **272**, 1921 (1997).

[31] J. Vinuesa and C. Joachim, Europhys. Lett. **33**, 635 (1996).

[32] M. Magoga and C. Joachim, Phys. Rev. B **56**, 4722 (1997).

[33] E. Dehan, P. Temple-Boyer, R. Henda, J. J. Pedroviejo, and E. Scheid, Thin Solid Films **266**, 14 (1995).